THERMO-MECHANICAL PROCESSING OF STEELS FOR SUSTAINABLE ENERGY UTILIZATION

Grain Refinement Mechanism in the CGHAZ of Ultra-High-Strength Structural Steel: A Critical Analysis of the Impacts of Prior Austenite Grain and Cooling Rates

LIBO WANG,[1] CHENGYANG HU [ID],[1,4] SIBO LI,[1] XIANGLIANG WAN,[1,2,5] MING ZHONG,[3] FENG HU,[1] SONGBO ZHOU,[1] GUANGQIANG LI,[2] and KAIMING WU[1]

1.—The State Key Laboratory of Refractories and Metallurgy, Collaborative Innovation Center for Advanced Steels, Wuhan University of Science and Technology, Wuhan 430081, China 2.—Key Laboratory for Ferrous Metallurgy and Resources Utilization of Ministry of Education, Wuhan University of Science and Technology, Wuhan 430081, China. 3.—School of Metallurgy, Northeastern University, Shenyang 110819, China. 4.—e-mail: huchengyang@wust.edu.cn. 5.—e-mail: wanxiangliang@wust.edu.cn

High heat input welding results in coarse prior austenite grains (PAGs) and slow cooling rates in the coarse-grained heat-affected zone (CGHAZ) of ultra-high-strength steel. High-temperature laser-scanning confocal microscopy and electron backscatter diffraction were used to accurately analyze the effects of PAG size and cooling rate at medium stage on bainite transformation behavior and grain refinement to combat the coarsened structure (bainite) and low, worse toughness in the CGHAZ. Higher heat inputs caused larger PAG size, slower cooling rate, coarser bainite crystallographic structures and lower CGHAZ toughness. Additionally, the austenite grains grew in opposite directions, collided and coalesced, and these were responsible for high-temperature grain coarsening. During cooling, austenite decomposed into bainite with a Kurdjumov–Sachs (K–S) relationship with PAGs, refining the crystallographic grain. Coarser PAG size slowed the bainite transformation and increased its size. Additionally, bainite nucleation rates and boundaries varied with cooling rates for the different variants. The CGHAZ with smaller PAGs and fast cooling rate exhibited an ultra-fine structure because the additional driving force increased the bainite random orientations. The PAG size strongly affected the bainite crystallographic grain size more than the cooling rate, indicating the size limit rather than the nucleation rate.

INTRODUCTION

In recent decades, for sustainable energy and reducing carbon emissions, ultra-high-strength steel (UHSS) has become an inevitable choice for offshore wind power installations.[1–3] UHSS, produced through a thermo-mechanical control process (TMCP), is used to make the floating wind power installations lighter and more suitable for further ocean depths.[1–4] High heat input welding is a necessary processing technology for offshore wind power installation manufacturing. The increase of heat input largely affects the mechanical properties of the welded joint, especially the cryogenic fracture toughness.[5,6] Extensive research has shown that the coarse-grained heat-affected zone (CGHAZ) is the location with the poorest fracture toughness in the welded joint.[7–9] Therefore, improving toughness in the CGHAZ of UHSS is urgently required, particularly at the weld joints experiencing high heat inputs.

Refining the grain size has been proved to be a crucial routine to improve the toughness of CGHAZ.[10–13] However, the higher heat input induced coarser the prior austenite grain (PAGs,

austenite grain after welding) formation due to higher peak temperatures (T_p) and longer austenitization duration.[14] The coarsening of PAGs and slow cooling rate allowed nucleation of the bainite grain boundary, making the crystallographic grain coarser and less effective at hindering the expansion of cracks in CGHAZ. Controlling the size of the PAGs and cooling rate significantly affects the final microstructure of the CGHAZ of UHSS, which is the key to grain refinement.[10–13] Additionally, controlling inclusions and changing chemical composition hinder the formation of acicular ferrite; the microstructure of the CGHAZ of UHSS is fully bainite.[15] Extensive research has studied the grain refinement mechanism in CGHAZ of UHSS. Wen et al.[12] reported that the microstructure of CGHAZ was characterized by complete martensite, a mixture microstructure (lath martensite and bainite) and granular bainite, respectively, with the increase of heat inputs. Yan et al.[13] found that small PAG size modified the microstructure of martensite-austenite (M-A) constituents from twin martensite to austenite, contributing to the improvement of $-20\,°C$ impact toughness from 60.20 J to 163.10 J. However, most of the previous studies on the grain refinement mechanism in steels were focused on PAG size or cooling rates. In fact, when the heat input increases, the PAG size increases, while the cooling rates at medium transformation temperatures also decrease. It is critical to investigate the dominant role of PAG size and cooling rate in forming fine-grained structures.

Investigating grain growth and microstructure transformation during welding often involves studying the room-temperature PAG size and microstructural characteristics of the samples after welding or thermal simulation. The current studies are not satisfied with characterizing the treated samples and focus on grain growth and microstructural transformation during welding.[16,17] High-temperature laser-scanning confocal microscopy (HTLSCM), under the protection of argon atmosphere by using halogen light source heating, which can observe the phase transformation and microstructural evolution of metal materials on a two-dimensional (2D) plane in situ. In situ real-time observation at high temperature has been extensively studied in the fields of metallurgy, materials and welding.[17] Austenite,[16] widmanstätten,[17] acicular ferrite,[18] bainite[19] and martensite[20] have been previously studied. As a covariant phase transformation product, the bainite structure has a predetermined orientation relationship with the PAGs,[21] leading to 24 variants[22] that can be classified into four groups based on their close-packed (CP) arrangement. Each CP group contains six variants exhibiting a parallel relationship of CP planes with the austenite. Alternatively, the 24 variants can be grouped based on three distinct variants of Bain groups.[23] The combination of electron backscatter diffraction (EBSD) and ARPGE[24] (a Python-based computer software leveraging the theoretical results given by GenOVa to automatically reconstruct the parent grains from EBSD data obtained on phase transition materials with or without residual parent phase) has been demonstrated as a valuable technique for analyzing samples exhibiting the bainite structure.

Hence, this study used HTLSCM to observe the behaviors of austenite growth and bainitic transformation in the simulated CGHAZ. Furthermore, variant selection mechanisms were investigated using EBSD under different PAG sizes and cooling rates during the bainitic transformation. The primary objective of this study was to explore the influence of PAG size and cooling rate on the grain refinement and impact on toughness of the CGHAZ in UHSS. Additionally, it aimed to provide satisfactory scenarios of welding parameters and guarantee the outstanding performance of the weld joint.

EXPERIMENTAL

Industrial-strength vacuum refining, continuous casting, hot rolling and tempering were used to produce a 30-mm-thick steel plate. The primary elements that made up this steel were 0.056C-0.23Si-1.62Mn-0.057Nb-0.21Cr-0.23Mo-0.0015B. The investigation focused on analyzing the microstructure and the corresponding fluctuations in impact toughness within the CGHAZ, which was achieved by replicating a welding thermal cycle using a thermo-mechanical simulator (Gleeble 3500). The welding thermal simulation sample was taken horizontally from the center of an F690 forged steel plate (F690) and was processed into a 100 mm × 11 mm × 11 mm sample. A 2D Rykalin mathematical model was used to determine the welding thermal cycle curves to simulate the welding process of 30-cm-thick plates. The heating rate was set at 200 °C/s to simulate different welding heating inputs (E). The T_p was 1350 °C, and the residence time was 1 s. As shown in Fig. 1a, the time of cooling the molten pool from 800 °C to 500 °C ($t_{8/5}$) was 4.9, 11.4, 16.2, 32.4, 64.2 and 129.7 s, which was equivalent to 15, 35, 50, 100, 200 and 400 kJ/cm in realistic welding, respectively. Each experiment was repeated five times, and the temperature was controlled using a K-type thermocouple wire, resulting in a 350 °C final temperature. The thermal simulation sample was processed into a 10 mm × 10 mm × 55 mm sample after the simulation thermal cycle using electric discharge machining (EDM), and the Charpy V-notch impact toughness was tested at $-20\,°C$. EBSD (Oxford symmetry) was used to describe the structural morphology and orientation of sample matrixes and investigate the impacted sample for lateral dissection of the crack.

Subsequently, cylinders with 5 mm diameter and 4 mm length were cut from the experimental steels and mounted in a $\Phi 9 \times 4\ mm^3$ alumina crucible. HTLSCM and infrared furnace imaging were used
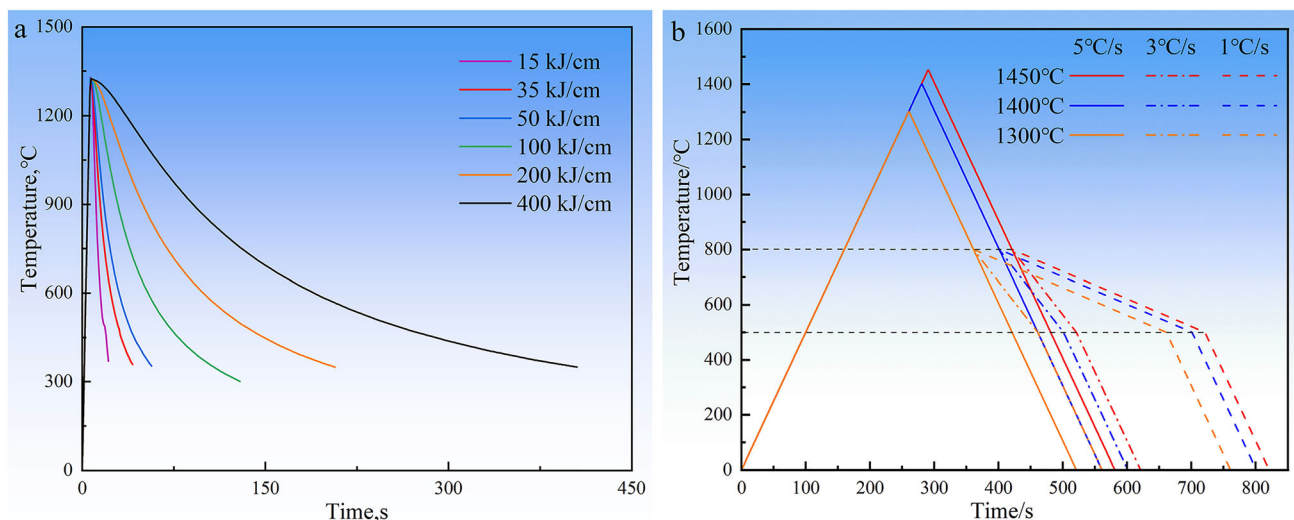
Fig. 1. Heating process diagram for (a) welding thermal cycle and (b) HTLSCM.

for in situ observation. The furnace temperature was measured using a thermocouple, which was accurate to within 0.1 °C, and was placed under the crucible. As shown in Fig. 1b, the samples were heated to 1300–1450 °C at a 5 °C/s rate and held there for 1 s for austenization, followed by rapid cooling to 800 °C at a 5 °C/s rate and cooling to 500 °C at 1, 3 and 5 °C/s rates. These parameters were selected based on Ref. 25. During the simulated thermal cycling, five photographs were taken per second to track the development of PAGs and their subsequent transformation into bainite. The heating and cooling rates (± 5 °C/s) in the simulated welding procedure were intentionally adjusted to be slower than in the rapid thermal cycle of actual welding involving high heat inputs to facilitate the examination of grain boundary migration at elevated temperatures. The mean linear intercept method was used to determine the average PAG size. After the heat treatment of the samples, the field previously investigated using HTLSCM was analyzed using EBSD through scanning electron microscopy (SEM, JEOL7000F) operated at 20 kV, with a 300 nm step size.

RESULTS

Microstructure and Impact Toughness in the Simulated CGHAZ Subjected to Various Heat Input Welding

The OM images of the experimental steels subjected to various simulated welding thermal cycles are shown in Fig. 2. The measured data showed that the average PAG sizes of the experimental steels grew larger with increased heat inputs. Heat inputs influence cooling rates, affecting the microstructure formation. Investigations have established a direct relationship between the heat input and cooling rate, and the cooling rate increased with the decrease in welding heat input.[25] As shown in Fig. 2a, non-diffusive bainite transformation occurred at a 15 kJ/cm heat input because of the rapid cooling rate. Thus, lath-type bainite constituted the microstructure in CGHAZ at 15 kJ/cm, respectively. As shown in Fig. 2b and c, austenite was transformed into lath-type bainite at a 35–50 kJ/cm heat input, similar to 15 kJ/cm, and the cooling rate slowed down. As shown in Fig. 2d–f, GB was formed at higher temperatures when the heat input was 100–400 kJ/cm because of the decreased cooling rate. Meanwhile, blocky M-A components were formed in the second phase. The retained austenite film could transform into M-A components because of carbon diffusion.

As shown in Fig. 3, PAG morphology was analyzed using EBSD, and the ARPGE algorithm was used to reconstruct and calibrate the austenite grain and bainite variants.[24] A close Kurdjumov–Sachs (K–S) relationship must be maintained with the parent austenite to theoretically form 24 different variants of bainite using variant selection.[22] The minimum misorientation between variant V1 and other variants is 10.5°.[22]

Therefore, a ≥ 10° misorientation at the boundary could indicate the boundary between two crystallographic grains of bainite blocks. Grains were assumed to be spherical to assess the grain size (Fig. 3c–f); no single Bain or CP group was found to dominate the PAGs with a heat input > 35 kJ/cm. The variants within the same Bain group exhibited proximity to each other at 35 kJ/cm, but the variants within the same CP group were formed in subdivided parts. The PAG is often combined with variants of the same Bain group (Fig. 3b). At 15 kJ/cm, the variants within the same CP group exhibited proximity, but variants within the same Bain
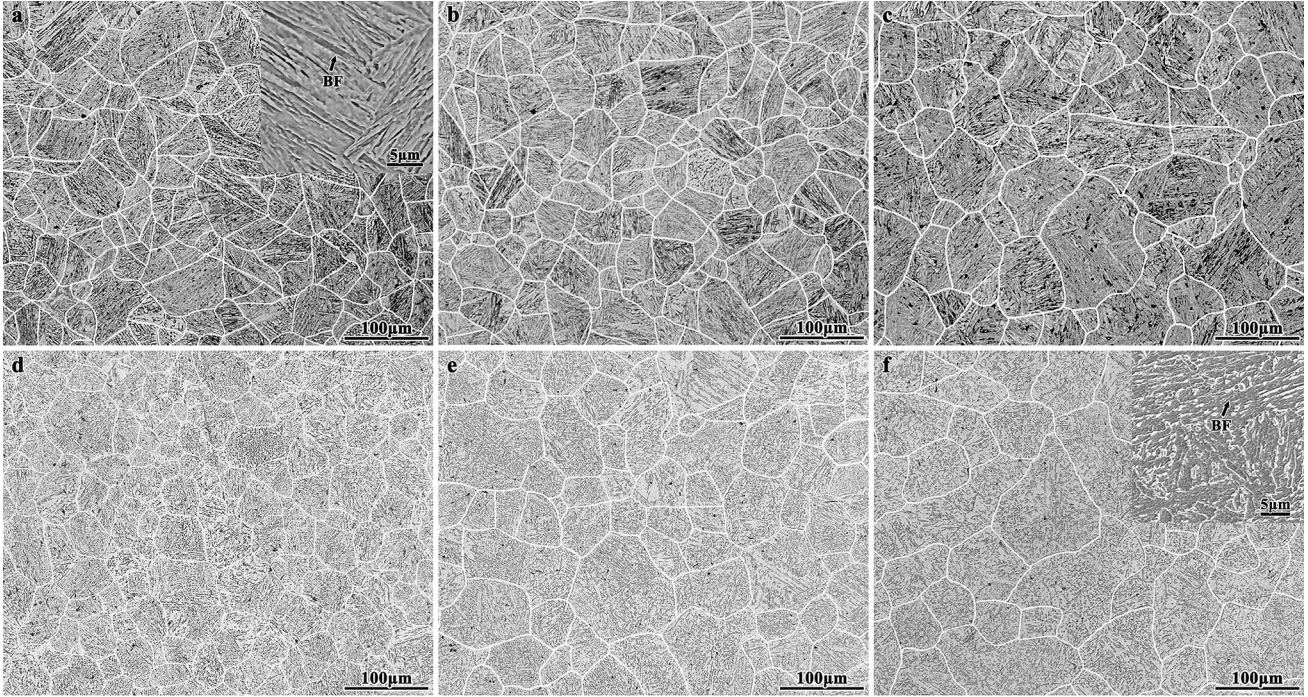
Fig. 2. Optical micrographs in the CGHAZ subjected to various welding heat inputs of (a)15 kJ/cm, (b) 35 kJ/cm, (c) 50 kJ/cm, (d) 100 kJ/cm, (e) 200 kJ/cm and (f) 400 kJ/cm (the inserted figures are obtained from SEM). BF = bainite ferrite.

group were divided into multiple parts. PAG combined primarily with variants from the same CP group (V1/V2/V3 in Fig. 3a). This finding illustrated that utilizing the 15 kJ/cm heat input resulted in a more robust variant selection than other heat inputs, yielding a substantial quantity of V1. Additionally, the same variant (V1) predominated within the internal structure of PAGs.

The statistical distribution of the mean equivalent grain diameters, crystallographic grain and impact toughness in CGHAZ is shown in Fig. 4. The mean PAG sizes in CGHAZ increased from 36.1 ± 1.1 to 74.9 ± 7.0 μm with the increased heat input, as shown in Fig. 4a. The crystallographic grain sizes of CGHAZ also increased and grew from 4.9 μm to 12.9 μm, as shown in Fig. 4b. However, the toughness of the experimental steels revealed contrasting tendencies, as shown in Fig. 4c. The Charpy impact absorbed energy decreased from 213 ± 11.0 J (15 kJ/cm) to only 5.1 ± 0.6 J (400 kJ/cm) at -20 °C. The misorientation and boundary density under different heat inputs are shown in Table I. The statistical results showed that the misorientation and boundary density of the high-angle grain boundaries (HAGBs) significantly decreased with increased heat input; especially the HAGBs dropped to 41% at 100 kJ/cm. This was consistent with the trend of decreased impact toughness.

Additionally, the crack morphology of the samples can explain and verify the difference in toughness generated because of the experimental steels. The

EBSD analysis results for the microstructure of crack propagation for the 100 kJ/cm simulated CGHAZ are shown as inverse-pole figure (IPF) images in Fig. 5. The SEM fracture morphology of impact samples at different multiples in Fig. 5a and b showed a typical cleavage fracture, with many cleavage planes and tearing edges distributed on the fracture surface. This study presupposed that the threshold for HAGBs was 10°, implying that a grain boundary exhibiting a misorientation $> 10°$ could be considered as the boundary between two distinct grains. As shown in Fig. 5c, the large volume of the block structure was readily apparent, and the cracks were distributed among the block structures. There were subtle color variations among bainite blocks, each indicating a slightly different orientation. The crack moved along the same or similar block, suggesting transgranular propagation. The crack would turn if it ran into a crystal with a different orientation. The crack progressed slowly and could turn easily when it reached the HAGBs. The obstructive effect was more pronounced as the density of the HAGBs increased. As shown in Fig. 5d, the crack easily passed through the low-angle grain boundaries (LAGBs) during propagation but ultimately stagnated at the HAGBs. Furthermore, the calculation of the proportion of variants showed that several V1 variants were dominating. As shown in the misorientation statistics in Fig. 5f, LAGBs dominated, and this was consistent with the results shown in
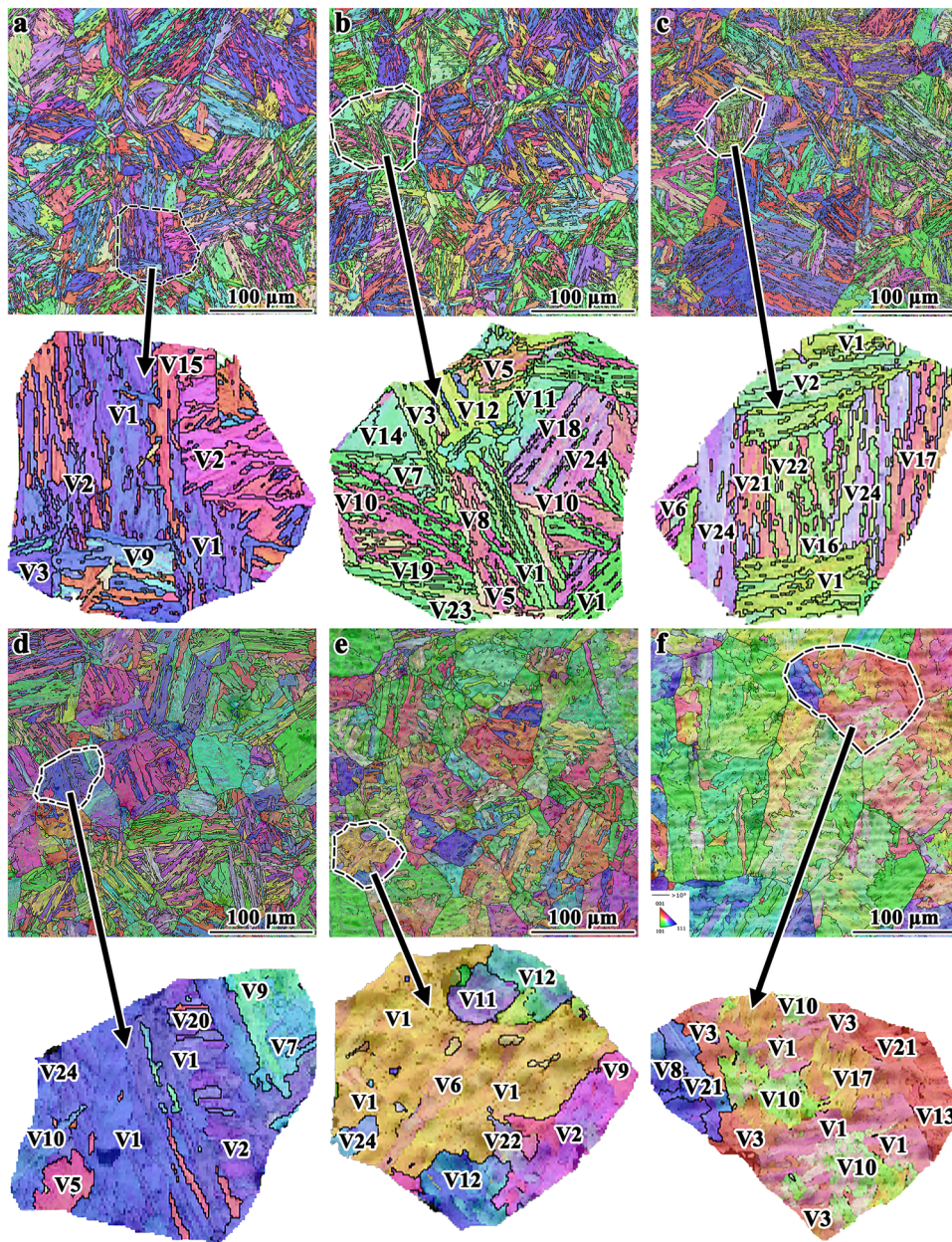
Fig. 3. EBSD analysis of microstructure in the CGHAZ subjected to various heat input welding. (a) 15 kJ/cm, (b) 35 kJ/cm, (c) 50 kJ/cm, (d) 100 kJ/cm, (e) 200 kJ/cm, (f) 400 kJ/cm.

Fig. 5d. Similar results could be observed in low-carbon bainitic weld metals.[26]

In situ Observation of Austenite Grain Growth and Bainite Transformation During Simulated Welding Thermal Cycles

The in situ observations of austenite grain growth in the experimental steel during heating, specifically during the $\alpha \rightarrow$ transformation, are shown in Fig. 6a–f. The dashed lines represent the grain boundaries. As shown in Fig. 6a–c, the α/γ interface of grain 1 was pushed outward, and it grew in an isotropic manner with increased temperature. As seen in Fig. 6d and e, small grains (grains 2–4) were

separated from the α-phase in the early transformation stage in the experimental steel. As shown in Fig. 6f, the grains were in contact with each other over time, progressively enveloping the entire surface.

The grain boundary migration after cooling from 1400 °C is shown in Fig. 6g–i. The austenite grain boundary expanded by a total of 47.6 μm with 0.7 μm/s velocity. Expansion of austenite grains was observed during heating, isothermal holding and cooling. The austenite grains ceased to grow on reaching a temperature $<$ 1050 °C during cooling. An increase in the size of austenite grains was observed with increased temperature or holding time.
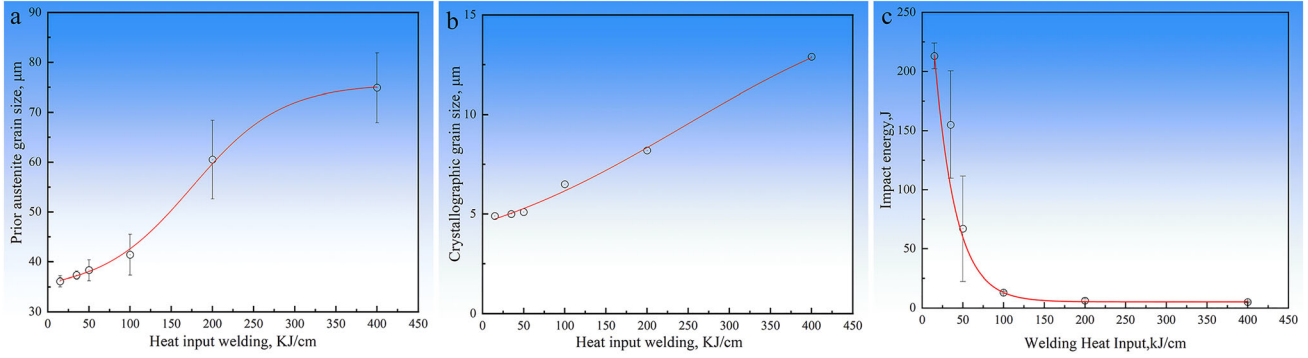
Fig. 4. Relation of heat input with (a) mean PAG size, (b) crystallographic grain size and (c) impact toughness in the CGHAZ of ultra-high-strength structural steel.

Table I. Statistics of misorientation in the CGHAZ of steels with various heat inputs

Sample	15 kJ/cm	35 kJ/cm	50 kJ/cm	100 kJ/cm	200 kJ/cm	400 kJ/cm
Misorientation (%)						
2°–10°	42	45	49	58	69	78
10°	58	55	51	41	31	22
Boundary density ($\mu m/\mu m^2$)	0.98	1.18	1.13	0.84	0.65	0.53

As shown in Fig. 7, the process of austenite decomposition to bainite within the CGHAZ was observed directly during the medium temperature stage using HTLSCM. The austenite microstructure is seen in Fig. 7a, where the arrowed-out black line denotes the grain boundary. Depicted as Bainite 1 in Fig. 7b, the bainite lath formation within block 1 primarily occurred at the austenite grain boundary and subsequently propagated into the grain. The same nucleation sites and growth directions in bainite laths parallelly align them. As seen in Fig. 7c, they rapidly grew until they collided with the austenite grain boundary, where their growth appeared to halt. Additionally, the secondary bainite (Bainite 3) was formed when the pre-existing bainite (Bainite 2) underwent sympathetic nucleation, as seen in Fig. 7e. The later formed bainite laths maintained a constant angle (43°) with Bainite 2 and grew in a block, as seen in Fig. 7f. Many bainite blocks were formed as the austenite decomposition proceeded because of primary and sympathetic nucleation. They grew in various directions and eventually collided. As shown in Fig. 7g–i, the expansive austenite grain was successfully partitioned into multiple smaller and distinguishable regions, constraining the expansion of subsequently formed bainite blocks. Consequently, it was clear that the length of those bainite blocks shrank as the temperature dropped.

EBSD Analysis and Variant Reconstruction

ARPGE was employed to reconstruct the austenite grain and calibrate the bainite variants, and this was done utilizing in situ HTLSCM observation and EBSD post-mortem in the same area after the transformation was complete. The outcomes in experimental steels are depicted in Fig. 8. The primary nucleation of the bainite block B1 occurred at the boundary between austenite grains and subsequently expanded into the interior of the grains. The formation of the bainite blocks B2 and B3 commenced at the boundary of the austenite grain and subsequently expanded in divergent directions towards the interior of the grain. Blocks B1 and B3 nucleated on opposite sides of boundaries and grew in the same direction, while the impingement on the earlier formed B1 apparently halted bainite formed later (B2), as shown in Fig. 8a2.

As shown in the pole figure and orientation map in Fig. 8a3, b3, and c3, multiple varieties of bainite, which were characterized by unique crystallographic orientations, developed within a single austenite grain. Additionally, a clear orientation relationship, either K–S or Nishiyama–Wassermann (N–W), was observed between the bainite variants and PAGs. Bainite blocks forming in the same austenite grain and growing in the same direction exhibited a high degree of similarity in their orientations and were denoted as B1 and B3. Conversely, bainite blocks developing within grains growing in opposite directions displayed distinct variant selections, specifically B1 and B2.

Finally, partitioning the large PAGs into numerous smaller regions using bainite with a wide range of variant selection achieved small crystallographic grains, as shown in Fig. 9. The results demonstrated that the bainite formation with distinct variants within larger austenite grains could significantly refine the final microstructure. The crystallographic
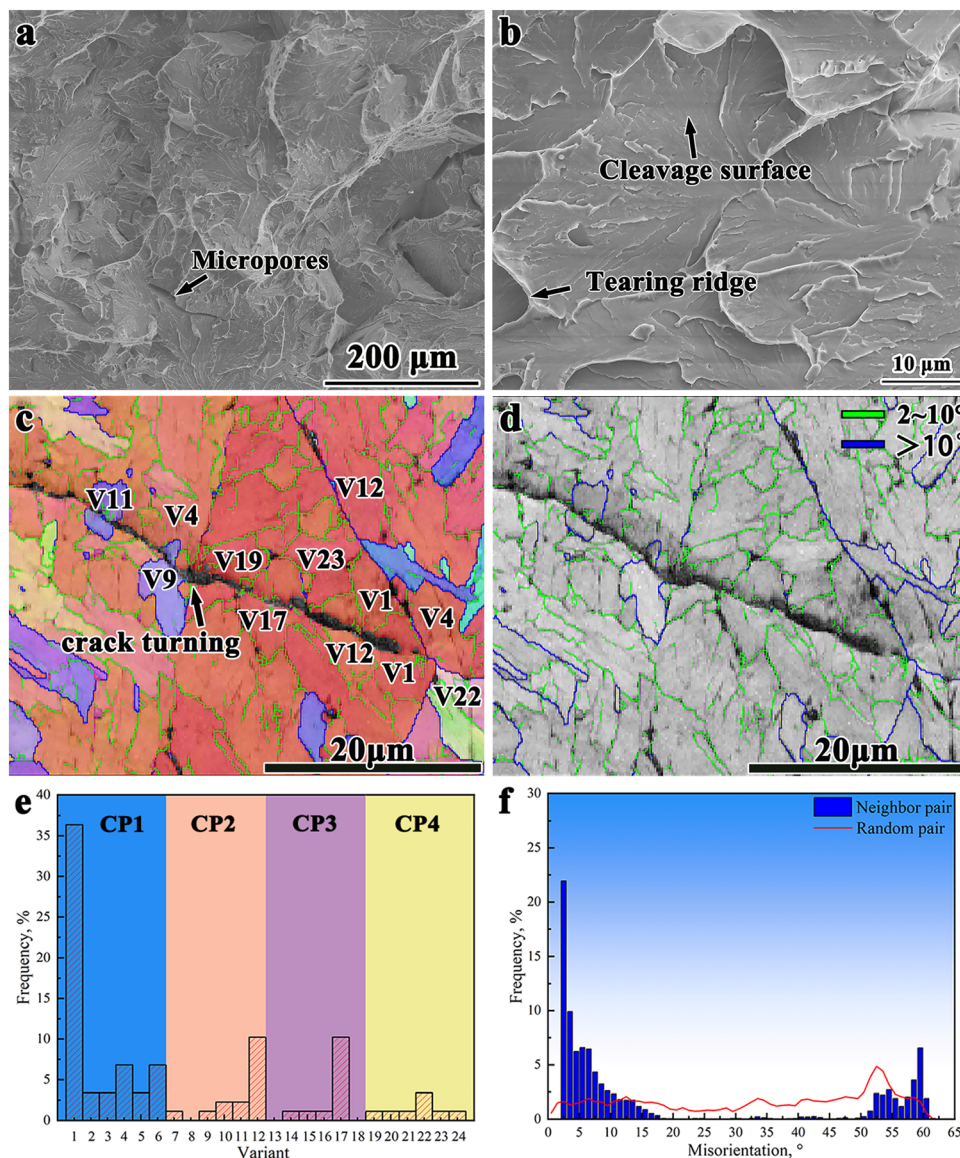
Fig. 5. SEM fracture morphology and EBSD analysis of crack propagation in the CGHAZ subjected to 100 kJ/cm heat input welding.

grain sizes in the CGHAZ of the experimental steel increased from 4.5 ± 4.0 to 10.5 ± 8.9 μm with raised T_p and lowered cooling rate.

DISCUSSION

Role of Welding Thermal Cycle on Austenite Grain Coarsening in the CGHAZ

The nucleation and growth processes involved in the $\alpha \rightarrow \gamma$ transformation have gained much attention in the welding of UHSS. As presented in Figs. 2, 3, 4 and 9, the PAG size increased with the climbing heat input and T_p. Furthermore, limiting the PAG size during welding is essential since coarser PAG resulted in larger crystallographic grain size, deteriorating the impact toughness in CGHAZ.

As shown in in situ observation results in this study in Fig. 6, austenite grains initially formed at

the α-phase boundary and migrated laterally along the α/γ interface, similar to previous studies.[16,27]

As expected, the transformation until completion involved the initiation of additional small grains and the subsequent enlargement of grains through their collisions. Following the $\alpha \rightarrow \gamma$ transformation, the presence of austenite grains characterized the microstructures of the samples. Some of the tiny grains of austenite coalesced to form larger ones when they were heated. The boundary of a sizable grain underwent displacement, swallowing the smaller neighboring grains.

Besides controlling the heat input (T_p and austenitization duration), particle pinning and solute-drag effect are the two methods to control the coarsening of PAG. The efficacy of grain-boundary pinning by the second-phase particles was observed, restricting the growth of austenite grains under the conditions
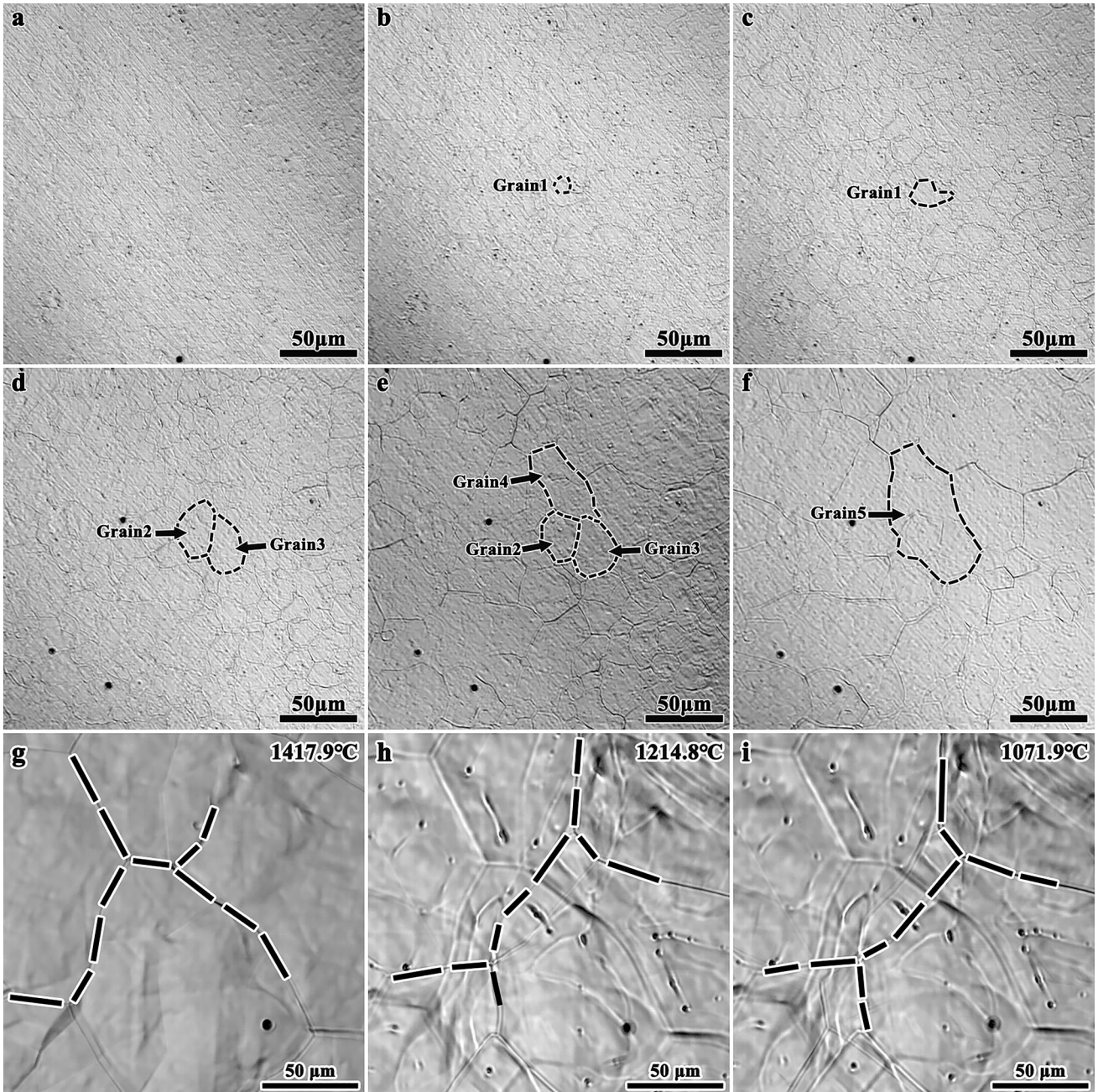
Fig. 6. In situ observation of austenite grain growth behavior during high temperature process. (a–c) Formation of austenite grain, (d–f) growth and impingement of austenite grain, and (g–i) migration of grain boundaries between austenite grains.

of rapid heating and short dwell time in austenite. The kinetic strength refers to the thermal energy produced by the thermal cycle and impacts various factors such as the rate of dissolution, precipitate size and density.[27–30] Notably, this influence was different from the equilibrium conditions.[30–34] An increase in Tp increased the kinetic strength for dissolving precipitation.

The observed correlation between the elevated dissolution temperature of Nb_xC_y precipitates and the improved resistance to grain coarsening was indicative. Additionally, it is well known that grain coarsening begins before the precipitates dissolve entirely.[35] The presence of precipitates before and after welding thermal simulation is shown in Fig. 10. The volume fraction of Nb_xC_y with temperature was calculated using Thermo-Calc. Temperature cycling with T_p values between 1190 °C and 1230 °C, corresponding to 35 to 15 kJ/cm heat inputs, completely dissolved the typical Nb_xC_y precipitates in experimental steel.[36] Moreover, the findings indicated that when exposed to temperatures exceeding T_p = 1168 and 1146 °C, accompanied by corresponding heat inputs of 15 and 35 kJ/cm, the precipitates would
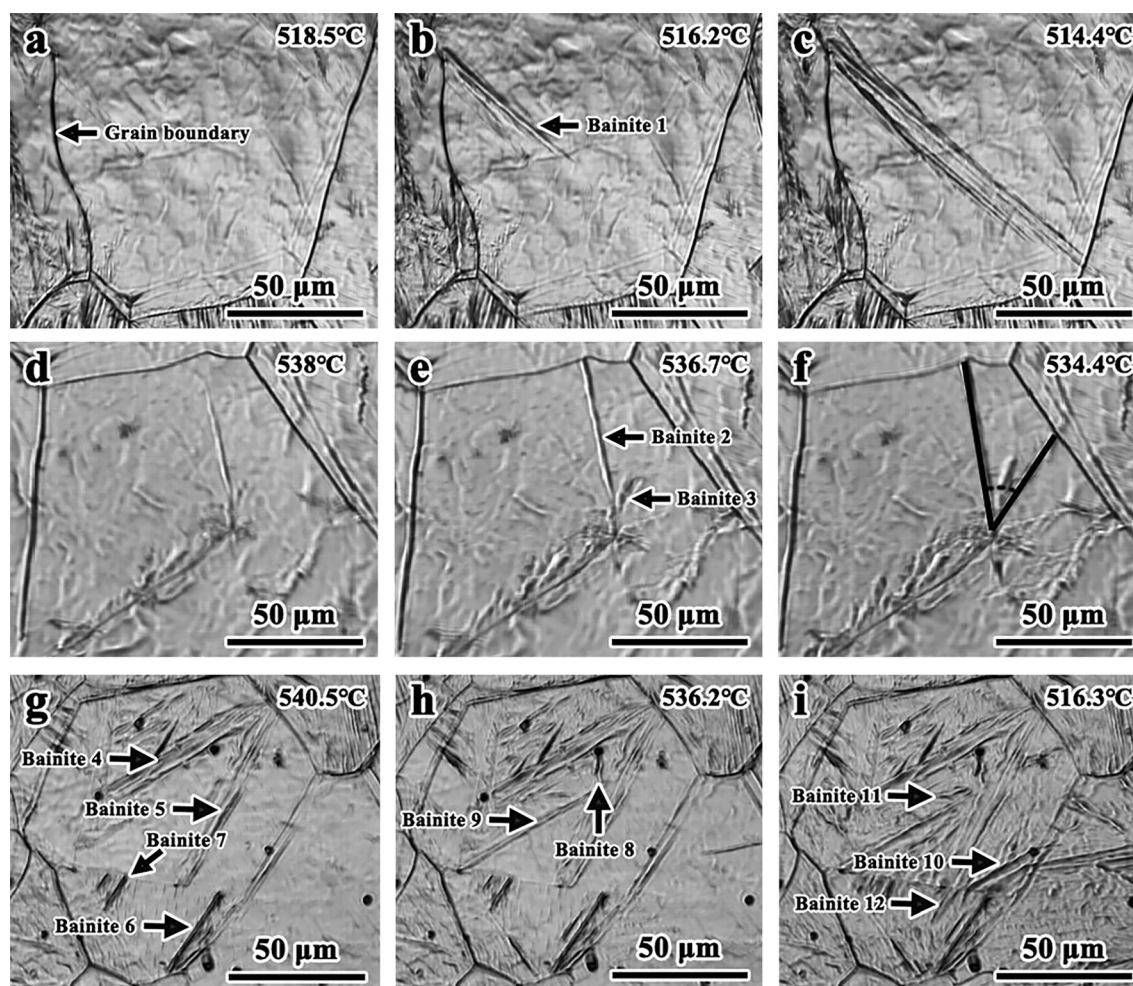
Fig. 7. In situ observation of bainite transformation behavior during medium temperature process. (a–c) Bainite nucleated at grain boundaries, (d–f) bainite nucleated at surface of bainite, and (g–i) the region was restricted by the impingement between the bainite.

undergo rapid dissolution. The precipitates grew to about 170 Å in diameter, the minimum size necessary to firmly pin the grain boundaries. The ability of precipitates to act as pins weakened as they became smaller than the critical size.

The austenite grain size in the CGHAZ exhibited a rapid increase with T_p across the entire 1100–1400 °C temperature range. As reported in previous isothermal heat-treatment studies, this phenomenon could be attributed to the lack of a significant solute-drag effect of Nb at elevated temperatures.[33,37] Thus, inducing the particle pinning effects to inhibit PAG coarsening to augment the impact toughness within the CGHAZ of UHSS is important for the higher heat input in actual welding.

Role of PAG Size and Cooling Rate on Bainite Transformation Behavior

Role of PAG Size on Bainite Transformation Behavior

PAG size governs the number of nucleation sites and growth rate, which significantly affects the morphological characteristics of bainite. On the one hand, the grain boundary area decreased with the increased austenite grain size, decreasing the nucleation sites. Thus, the sample with the larger austenite grains took longer to nucleate. On the other hand, the coarse austenite grain samples were wider and longer, giving more space for bainite growth.

As shown in Figs. 3, 4, 9 and 11, the coarsening of PAG led to a slower bainite transformation rate and a larger bainite size. The PAG size strongly impacted the crystallographic grain size in bainite because the PAG size inhibited the bainite size limit. The coarser PAG refinement substantially accelerated the bainite transformation rate since the process of grain refinement augmented the number of nucleation sites on the surface of austenite grains. Consequently, the increased nucleation sites resulted in a higher free energy change during the austenite transformation. Thus, the smaller PAGs exhibited an ultra-fine structure since the additional driving force produced more random orientations of bainite.
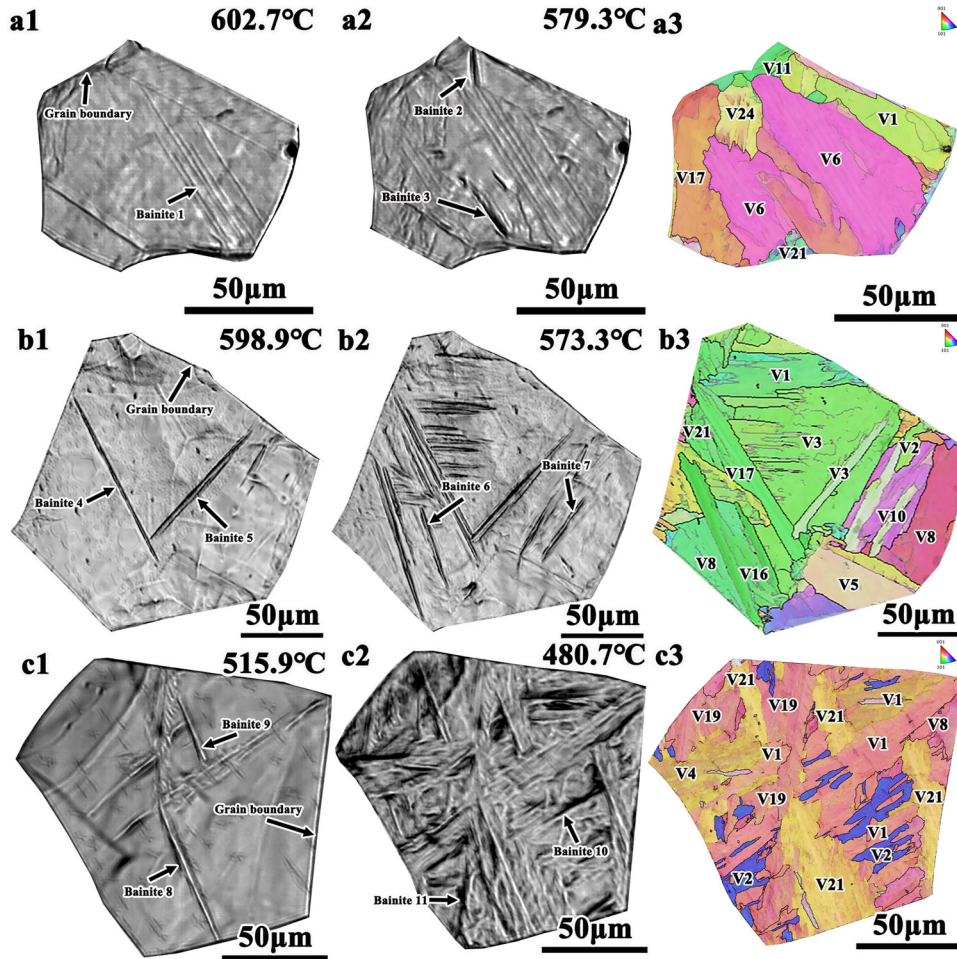
Fig. 8. (a–c) In situ observation of bainite transformation, respectively. (a1, a2, b1, b2, c1, c2) HTLSCM. The different variants in (a3, b3, c3) indicate the different bainite packets.

Role of Cooling Rate on Bainite Transformation Behavior

The nucleation and growth processes involved in bainite transformation have gained much attention in the processing of modern UHSS.[38] Numerous studies demonstrated that the bainite formation arising from the undercooled austenite transformation was a coherent and diffusion-driven process that took place at an intermediate temperature. The supercooling degree was associated with the cooling rate. Thus, the actual transformation temperature was lower, and the undercooling was greater for faster cooling rates.[39,40] The variant selection rule[41] established the initial orientation of bainite nucleated at the austenite grain boundary. Crystals with the same crystallographic orientation and the same habit plane are characterized as belonging to the Bain group and CP group, respectively.[42] The variant selection was seen at varying heat inputs in Figs. 3, 5, 8 and 9, consistent with the findings of previous studies.[41]

Heat input affects variant selection and pairing in CGHAZ, resulting in varying densities of HAGBs.

Previous studies showed a substantial correlation between the variant pairing and transformation strain, which was generated during shear transformation and stored in transformation products.[43] Heat input > 35 kJ/cm resulted in negligible transformation stress. Bainite formation readily accommodated plastic deformation at low driving forces.

The formation of variants belonging to the same Bain group occurred near each other because of the low transformation strain observed in this study (Fig. 3). A correlation where the decrease in heat input increased the transformation stress was observed when the heat input was reduced to 15 kJ/cm. Consequently, this necessitated a greater capacity for accumulating transformation stress in the resulting transformation products. As reported earlier, the V1/V2 variation pair with a 60° misorientation angle was the best choice for accommodating the transformation strain.[44] Furthermore, the variants within the same Bain group exhibited separation, and variants within the same CP group tended to form adjacent to each other (Fig. 3a). Morito et al. showed that the transformation strain could be effectively accommodated in a variant
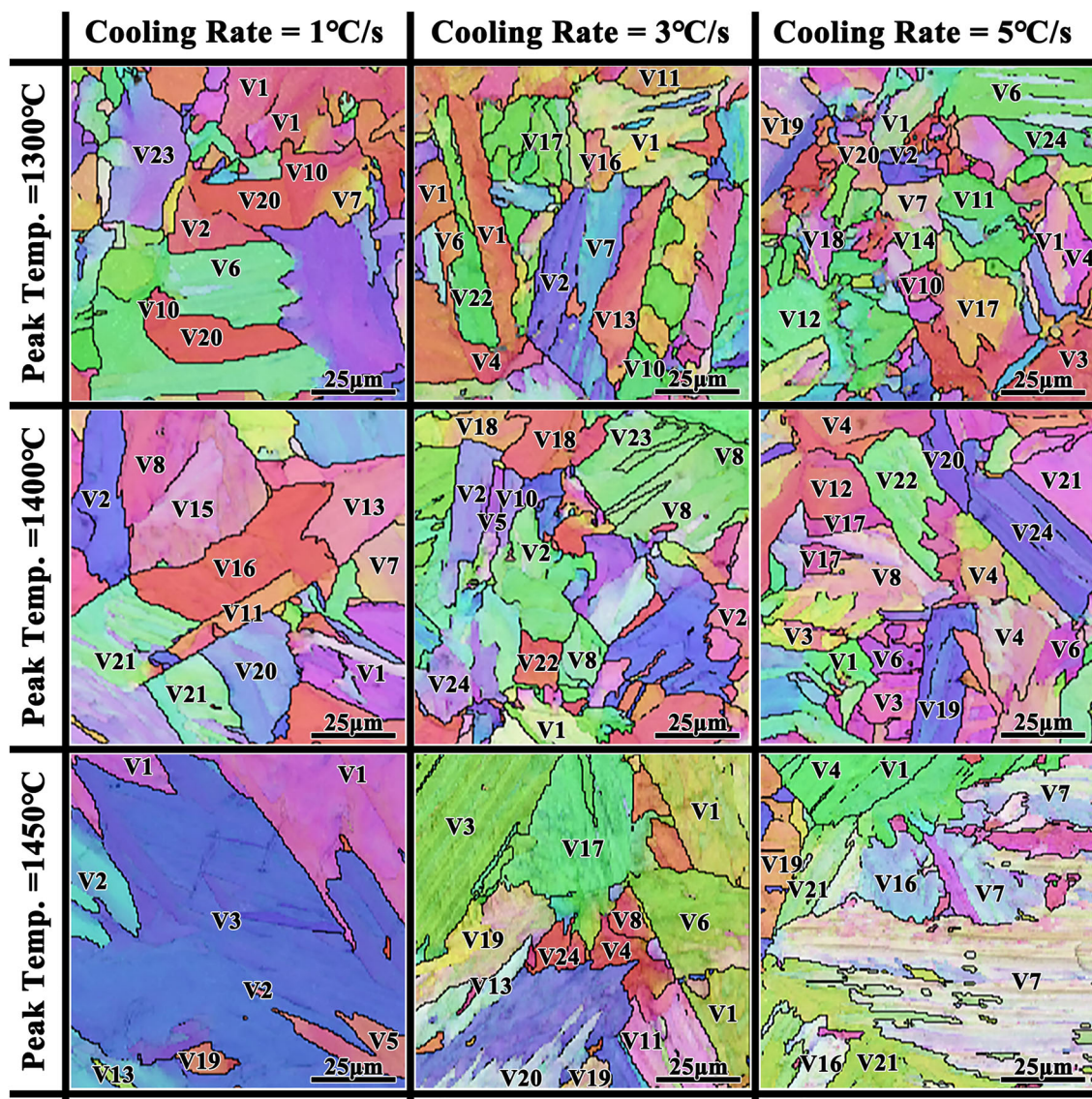
Fig. 9. IPF maps of BCC phases in the CGHAZ of investigated steels with various peak temperatures and cooling rates.

pair.[44] Furthermore, they observed that a variant pair of the same variants exhibited the best transformation strain among all possible combinations of variant pairs. Additionally, the formation of all six variants within the same CP group could facilitate a reduction in the transformation strain, indicating that a more robust variant selection process could effectively accommodate a greater amount of transformation strain. This study elucidated the rationale behind the enhanced variant selection at 15 kJ/cm, as shown in Fig. 3a. It was possible to observe a variant pair consisting of V1 and V2[23,44,45] and a variant pair consisting of V1 and V4[44,46] in martensite, increasing the density of HAGBs. The V1/V13/V24 variant pair predominated at ≥ 35 kJ/cm heat inputs. In this case, the low density of the HAGBs was because the variants belonging to the same Bain group exhibited a comparable crystallographic orientation. Consequently, the misorientation between them was smaller, < 15°. The comparison of the V1/V2 pair at 15 kJ/cm with the other two variant pairs showed that both these pairs increased the formation of LAGBs and decreased the density of HAGBs. Consequently, the abundance of HAGBs formed by multiple variants refined the crystallographic grain size in the bainitic microstructure.

As shown in Figs. 9 and 11, the samples with the same T_p but different cooling rates obtained different variants. A high T_p of 1450 °C and slow cooling rate of 1 °C/s achieved coarser variants compared to other specimens. Contrarily, the refinement ratio showed high T_p but the rapid cooling rate was much higher than for other specimens. Primarily, the cooling rate influenced the diffusion distance of interstitial element C and other alloying elements.
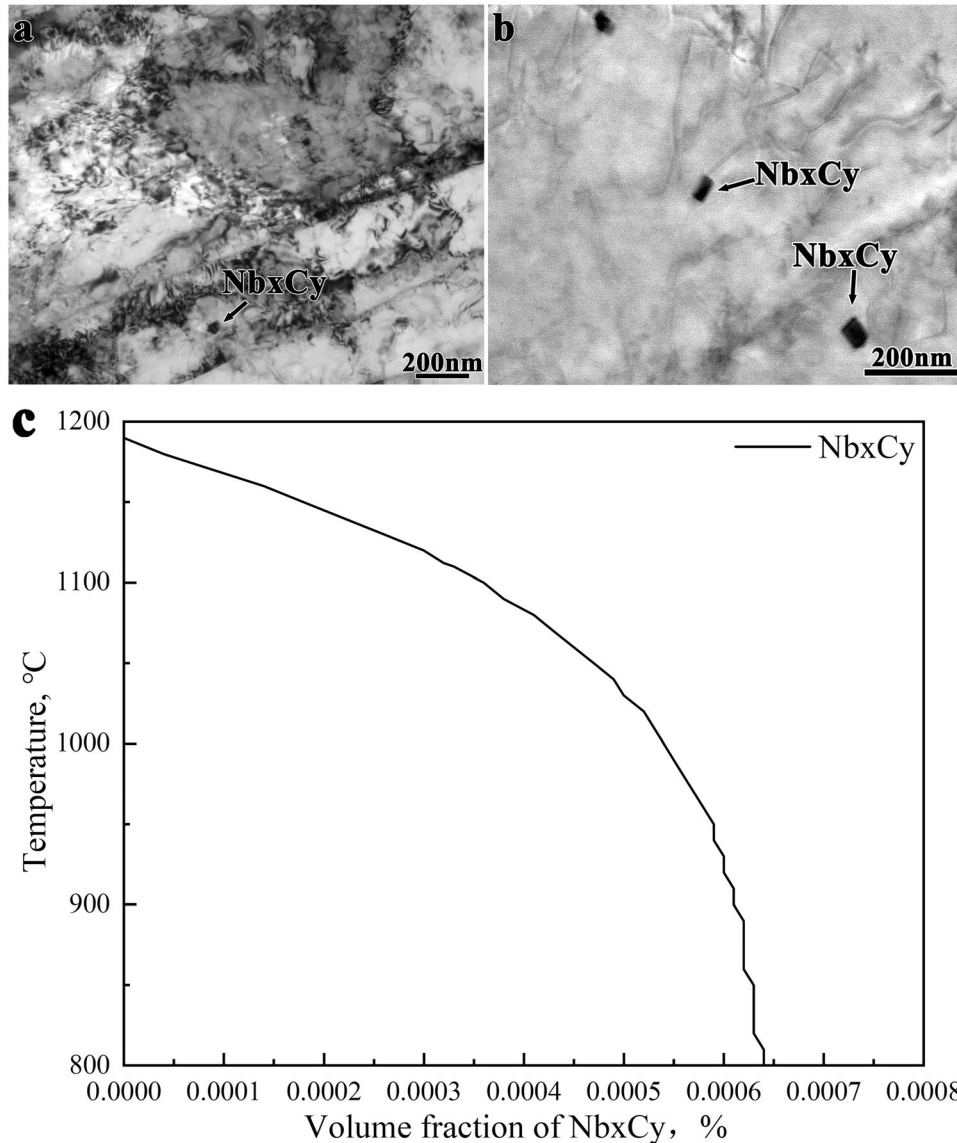
Fig. 10. TEM morphology and volume fraction of the content of Nb_xC_y particles varying with temperature. (a) Base metal; (b) 100 kJ/cm sample.

Consequently, this impacted the actual phase transformation temperature, leading to various phase transformations.[46–49] The slower cooling rate for the same T_p made it easier to form block boundaries than the rapid cooling rate.[50] The effect of different boundaries on the impact of toughness is discussed in detail in the next section.

In summary, different cooling rates due to heat inputs led to distinct microstructures, especially when the PAG was coarser than 70 μm. As shown in Figs. 2 and 4a, the mean PAG size was increased with the gradual increase in heat input. As shown in Fig. 4 and 11, $t_{8/5}$ had a weaker influence on the crystallographic grain size for small PAG sizes. However, as shown in Fig. 11, $t_{8/5}$ had a clear effect on the crystallographic grain size for large PAG size (> 70 μm), suggesting a positive correlation between them.

Impact of Grain Refinement on Impact Toughness

It is widely accepted that the microstructure significantly impacts the mechanical properties of the CGHAZ. Refining the grain size of the CGHAZ in UHSS is crucial for enhancing its properties. Excellent yield strength due to the barrier to dislocation movement for HAGBs is reflected in the well-known Hall-Petch relationship.[51] Materials with fine-grained bainitic microstructures featuring extensive impingements and intersections showed superior toughness when subjected to an impact test.[52] HAGBs could alter the cleavage crack propagation path and absorb more energy since they act as obstacles.[53] Thus, the CGHAZ of UHSS benefited from the fine-grained microstructure of bainite with abundant HAGBs, resulting in combined high yield strength and superior impact toughness.[54,55]
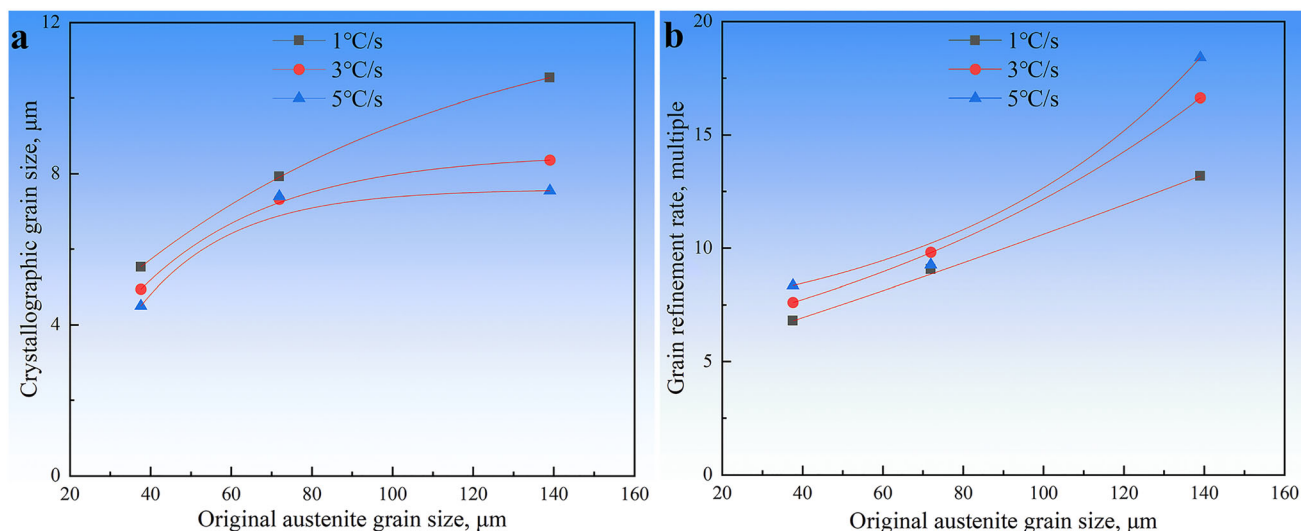
Fig. 11. Relation of PAG size and cooling rate with (a) crystallographic grain size and (b) grain refinement ratio in CGHAZ of ultra-high-strength steel.

M-A constituents and the distribution of grain boundaries influenced the impact toughness of the CGHAZ.[56] However, M-A constituents exhibited a reduced influence on impact toughness.[57] Therefore, the correlation between the distribution of bainite variants grain boundaries and the impact toughness was examined (Table I and Fig. 4c). The classification of grain boundaries depends upon the specific bainite variant pairs being compared. These boundaries could be categorized as sub-block boundaries, existing between the variants within the same CP group and Bain group. Additionally, block boundaries and packet boundaries were present between variants belonging to different Bain and CP groups, respectively. Wu et al.[57] showed that several V1/V2 variant pairs could be formed as the driving force of transformation increases, ensuring a high-density distribution of HAGBs. The impact absorbed energy decreased for increased heat input in CGHAZ (Table I and Fig. 4c). The heat input was inversely related to the total grain boundary density, and the density decreased with increased heat input. Among boundaries between different bainite variants, the sub-block boundary showed trends identical to the total grain boundary. The V1/V2 variant contributed to the high-density and high angle grain boundaries, significantly improving overall toughness. Although the packet boundary density and heat input had little to no correlation, the density of the block boundary decreased with the increased heat input (Figs. 3, 8 and 9).

Previous studies suggested a connection between the packet size and impact absorbed energy, and the block size was linked to yield strength.[58,59] Other studies showed that block size and packet size were the two most important variables in determining impact absorbed energy.[60] Additionally, previous studies demonstrated that HAGBs (> 45°) slowed

the crack propagation.[61] Consequently, all block boundaries and some packet boundaries (> 45°) acted as effective grain boundaries, affecting the impact absorbed energy. Moreover, the higher density of effective grain boundaries resulted in superior impact toughness.

CONCLUSIONS

1. The austenite grains grew in various directions and collided with each other, coalescing the small grains. These phenomena were responsible for the grain coarsening in the high-temperature stage. The austenite decomposed into a bainite structure with a specific K–S relationship with PAGs during cooling, refining the crystallographic grain.
2. The variant selection got weaker with the increased heat input. Most variant pairs were equal to V1/V2 at 15 kJ/cm heat input and V1/V13/V24 at ≥ 35 kJ/cm heat input. V1/V2 promoted the formation of HAGBs compared to the other variant pairs, increasing the block boundaries that are attributed to superior impact toughness.
3. The PAG size predominantly affected the impact toughness in CGHAZ. Coarser PAG size of 140 μm implied coarser crystallographic grain size (>7 μm) in bainite when the other conditions were similar since it slowed the bainite transformation rate and coarsened the bainite size. Furthermore, the cooling rate was important for a sufficiently large PAG size (> 70 μm) since it determined the bainite nucleation rate and the boundary types among different variants, which were attributed to the driving force and free energy change during the bainite transformation.

ACKNOWLEDGEMENTS

CONFLICT OF INTEREST

On behalf of all authors, the corresponding author states that there is no conflict of interest.

REFERENCES

1. D.K. Liu, J. Yang, Y.H. Zhang, and L.Y. Xu, *J. Iron. Steel Res. Int.* 29, 846 https://doi.org/10.1007/s42243-021-00639-6 (2022).
2. X.L. Gan, X.L. Wan, Y.J. Zhang, H.H. Wang, G.Q. Li, G. Xu, and K.M. Wu, *Mater Charact.* https://doi.org/10.1016/j.matchar.2019.109893 (2019).
3. Y.W. Wu, X.B. Yuan, I. Kaldre, M. Zhong, Z.J. Wang, and C. Wang, *Metall. Mater. Trans. B* 54, 50 https://doi.org/10.1007/s11663-022-02697-x (2023).
4. B.B. Rath, *JOM* 61, 73 https://doi.org/10.1007/s11837-009-0056-0 (2009).
5. J.C. Sun, X.D. Zou, H. Matsuura, and C. Wang, *JOM* 70, 946 https://doi.org/10.1007/s11837-018-2824-1 (2018).
6. X.B. Yuan, M. Zhong, Y.W. Wu, and C. Wang, *Metall. Mater. Trans. B* 53, 656 https://doi.org/10.1007/s11663-022-02455-z (2022).
7. L.P. Nishikawa, and H. Goldenstein, *Jom-Us* 71, 815 https://doi.org/10.1007/s11837-018-3213-5 (2019).
8. M. Shome, *Mater. Sci. Eng. A* 445, 454 https://doi.org/10.1016/j.msea.2006.09.085 (2007).
9. R. Cao, J. Li, D.S. Liu, J.Y. Ma, and J.H. Chen, *Metall. Mat Trans. A* 46, 2999 https://doi.org/10.1007/s11661-015-2916-2 (2015).
10. X. Guo, S. Liu, J. Xu, S. Wang, L. Fu, Z. Chai, and H. Lu, *Mater. Sci. Eng. A.* https://doi.org/10.1016/j.msea.2021.141827 (2021).
11. W.J. Liu, H.Y. Li, W.H. Zhou, D. Luo, D. Liu, L. Liang, and A.D. Xiao, *Materials (Basel).* https://doi.org/10.3390/ma16020581 (2023).
12. C. Wen, Z. Wang, X. Deng, G. Wang, and R.D.K. Misra, *Steel Res. Int.* 89, 55 https://doi.org/10.1002/srin.201700500 (2018).
13. W. Yan, X. Luo, G. Xu, H. Wang, Z. Wang, and X. Chen, *Mater. Sci. Eng. A.* https://doi.org/10.1016/j.msea.2022.142725 (2022).
14. O. Amelirad, A. Assempour, J. Manuf. Process. https://doi.org/10.1016/j.jmapro.2019.09.035 (2019).
15. D.J. Abson, *Sci. Technol. Weld Joi* 23, 635 https://doi.org/10.1080/13621718.2018.1461992 (2018).
16. X.I. Wan, K.M. Wu, G. Huang, R. Wei, and L. Cheng, *Int. J. Min. Met Mater.* 21, 878 https://doi.org/10.1007/s12613-014-0984-8 (2014).
17. L. Cheng, K.M. Wu, X.L. Wan, and R. Wei, *Mater Charact* 87, 86 https://doi.org/10.1016/j.matchar.2013.11.002 (2014).
18. W. Bin, and S. Bo, *Steel Res. Int.* 83, 487 https://doi.org/10.1002/srin.201100266 (2012).
19. H. Hu, G. Xu, M. Nabeel, N. Dogan, and H.S. Zurob, *Metall. Mater. Trans. A* 52, 817 https://doi.org/10.1007/s11661-020-06109-0 (2021).
20. J. Tian, G. Xu, Z. Jiang, H. Hu, Q. Yuan, and X. Wan, *Met. Mater. Int.* 26, 961 https://doi.org/10.1007/s12540-019-00370-8 (2019).
21. Z. Guo, C.S. Lee, and J.W. Morris, *Acta Mater.* 52, 5511 https://doi.org/10.1016/j.actamat.2004.08.011 (2004).
22. T. Kaneshita, G. Miyamoto, and T. Furuhara, *Acta Mater.* 127, 368 https://doi.org/10.1016/j.actamat.2017.01.035 (2017).
23. T. Furuhara, H. Kawata, S. Morito, and T. Maki, *Mater. Sci. Eng. A* 431, 228 https://doi.org/10.1016/j.msea.2006.06.032 (2006).
24. C. Cayron, *J. Appl. Crystallogr.* 40, 1183 https://doi.org/10.1107/s0021889807048777 (2007).
25. L. Wang, C. Hu, X. Wan, S. Zhou, R. Wei, C. Zhu, G. Li, and K. Wu, *Sci Technol Weld Joi* 28, 608 https://doi.org/10.1080/13621718.2023.2189365 (2023).
26. G. Mao, C. Cayron, R. Cao, R. Logé, and J. Chen, *Mater Charact* 145, 516 https://doi.org/10.1016/j.matchar.2018.09.012 (2018).
27. H. Chen, E. Gamsjäger, S. Schider, H. Khanbareh, and S. van der Zwaag, *Acta Mater.* 61, 2414 https://doi.org/10.1016/j.actamat.2013.01.013 (2013).
28. J.C. Ion, K.E. Easterling and M.F. Ashby, Acta Metall (1984).
29. M.F. Ashby, and K.E. Easterling, *Acta Metall.* 30, 1969 https://doi.org/10.1016/0001-6160(82)90100-6 (1982).
30. N. Ryum, I. Andersen, O. Grong, and I. Andersen, *Acta Metall.* 43, 2689 https://doi.org/10.1016/0956-7151(94)00489-5 (1995).
31. J.A. Wert, *JOM* 34, 35 https://doi.org/10.1007/bf03338094 (1982).
32. L.J. Cuddy, and J.C. Raley, *Metall. Trans. A* 14, 1989 https://doi.org/10.1007/bf02662366 (1983).
33. E.J. Palmiere, C.I. Garcia, and A.J.D. Ardo, *Metall. Mater. Trans. A* 25, 277 https://doi.org/10.1007/bf02647973 (1994).
34. P.A. Manohar, D.P. Dunne, T. Chandra, and C.R. Killmore, *ISIJ Int.* 36, 194 https://doi.org/10.2355/isijinternational.36.194 (1996).
35. M. Shome, O.P. Gupta, and O.N. Mohanty, *Met Mater Trans A* 35, 985 https://doi.org/10.1007/s11661-004-0025-8 (2004).
36. M. Shome, D.S. Sarma, O.P. Gupta, and O.N. Mohanty, *ISIJ Int.* 43, 1431 https://doi.org/10.2355/isijinternational.43.1431 (2003).
37. T.A. Kop, P.G.W. Remijn, J. Sietsma, and S. van der Zwaag, *Materi Sci Forum* 284–286, 193 https://doi.org/10.4028/www.scientific.net/MSF.284-286.193 (1998).
38. H.K.D.H. Bhadeshia, Bainite in Steels (1992).
39. D.G. Brandon, B. Ralph, S.T. Ranganathan, and M.S. Wald, *Acta Metall.* 12, 813 https://doi.org/10.1016/0001-6160(64)90175-0 (1964).
40. H.I. Aaronson, G. Spanos, R.A. Masamura, R.G. Vardiman, D.W. Moon, E.S.K. Menon, and M.G. Hall, *Mater. Sci. Eng. B* 32, 107 https://doi.org/10.1016/0921-5107(95)80022-0 (1995).
41. Y. You, C. Shang, W. Nie, and S. Subramanian, *Mater. Sci. Eng. A* 558, 692 https://doi.org/10.1016/j.msea.2012.08.077 (2012).
42. X. Zhang, G. Miyamoto, Y. Toji, S. Nambu, T. Koseki, and T. Furuhara, *Acta Mater.* 144, 601 https://doi.org/10.1016/j.actamat.2017.11.003 (2018).

43. A.F. Gourgues, A. Pineau, and A. Lambert-Perlade, *Acta Mater.* 52, 2337 https://doi.org/10.1016/j.actamat.2004.01.025 (2004).
44. S. Morito, H. Tanaka, R. Konishi, T. Furuhara, and T. Maki, *Acta Mater.* 51, 1789 https://doi.org/10.1016/s1359-6454(02)00577-3 (2003).
45. M. Zhang, and P.M. Kelly, *Scripta Mater.* 47, 749 https://doi.org/10.1016/s1359-6462(02)00196-3 (2002).
46. N. Takayama, G. Miyamoto, and T. Furuhara, *Solid State Phenom.* 172–174, 155 https://doi.org/10.4028/www.scientific.net/SSP.172-174.155 (2011).
47. S.Q. Zhang, X.F. Hu, H.C. Jiang, and L.J. Rong, *Acta Metall Sin-Engl* 35, 1862 (2022).
48. I. Baik Sung, M.J. Olszta, S.M. Bruemmer, and N. Seidman David, *Scripta Mater.* 66(10), 809 https://doi.org/10.1016/j.scriptamat.2012.02.014 (2012).
49. M. Mizouchi, Y. Yamazaki, Y. Iijima, and A. Koji, *Mater. Trans.* 45(10), 2945 https://doi.org/10.2320/matertrans.45.2945 (2004).
50. E.O. Hall, *Proc. Phys. Soc. Sect. B* 64, 747 https://doi.org/10.1088/0370-1301/64/9/303 (1951).
51. J.R. Yang, C.Y. Huang, C.F. Huang, and J.N. Aoh, *J. Mater. Sci. Lett.* 12, 1290 https://doi.org/10.1007/bf00506341 (1993).
52. S.Y. Han, S.Y. Shin, S. Lee, N.J. Kim, J.-H. Bae, and K. Kim, *Metall. Mater. Trans. A* 41, 329 https://doi.org/10.1007/s11661-009-0135-4 (2010).
53. H. Wang, G. Li, X. Wan, H. Wang, K. Nune, Y. Li, and K. Wu, *Sci Technol Weld Joi* 22, 133 https://doi.org/10.1080/13621718.2016.1204774 (2017).
54. H. Yan, K. Wu, H. Wang, L. Li, Y. Yin, and N. Wu, *Sci Technol Weld Joi* 19, 355 https://doi.org/10.1179/1362171814y.0000000201 (2014).
55. L. Lan, X. Kong, and C. Qiu, *Mater Charact* 105, 95 https://doi.org/10.1016/j.matchar.2015.05.010 (2015).
56. X. Li, X. Ma, S. Subramanian, R. Misra, and C. Shang, *Metall Mater Trans E* 2, 1 https://doi.org/10.1007/s40553-014-0036-3 (2015).
57. B. Wu, Z. Wang, Y. Yu, X. Wang, C. Shang, and R. Misra, *Mater. Sci. Eng. A* 170, 43 https://doi.org/10.1016/j.scriptamat.2019.05.016 (2019).
58. S. Morito, H. Yoshida, T. Maki, and X. Huang, *Mater. Sci. Eng. A* 438–440, 237 https://doi.org/10.1016/j.msea.2005.12.048 (2006).
59. L. Rancel, M. Gómez, S.F. Medina, and I. Gutierrez, *Mater. Sci. Eng. A* 530, 21 https://doi.org/10.1016/j.msea.2011.09.001 (2011).
60. M. Abbasi, D.-I. Kim, T.W. Nelson, and M. Abbasi, *Mater Charact* 95, 219 https://doi.org/10.1016/j.matchar.2014.06.023 (2014).
61. H. Wang, Y. Tian, Q. Ye, R. Misra, Z. Wang, and G. Wang, *Mater. Sci. Eng. A* 761, 138009 https://doi.org/10.1016/j.msea.2019.06.019 (2019).